An Effective Antenna Pattern Reconstruction Method for Planar Near-Field Measurement System

Junhao Zheng, Xiaoming Chen, *Senior Member, IEEE*, and Yi Huang, *Fellow, IEEE*

***Abstract*—This article presents a method of antenna radiation pattern reconstruction for the planar near-field measurement system. The proposed method uses clustering analysis and Voronoi cell classification to realize reasonable regional interpolation according to the data characteristics of a small number of initial samples, leading to an expansion of the amount of effective data in the initial array. Meanwhile, the Gerchberg-Papoulis (GP) algorithm is used to reduce the truncation errors of the interpolated planar near-field data, and consequently improve the overall reconstruction accuracy. The proposed method can effectively reduce the number of initial sampling points and the planar near-field scanning time of the measurement process. Besides, it can be seen from the simulation and measurement results that the planar near-field data processed by the clustering interpolation and GP algorithm can effectively enhance the reconstruction accuracy of the far-field pattern of the antenna under test.**

***Index Terms*—Planar near-field measurement, clustering interpolation, Voronoi tessellation, Gerchberg-Papoulis algorithm, pattern reconstruction.**

I. Introduction

PLANAR near-field measurement system can obtain the radiation characteristics of the antenna under test (AUT) in a compact testing environment (cf. Fig. 1). So it has been widely used in antenna measurements. In order to obtain the planar near-field electric field data with small truncation errors, it is usually necessary to scan over a large aperture with dense sampling points in the near-field of the tested devices. However, in most cases, the measurement range and accuracy of the testing instrument are limited, resulting in fixed scanning areas and sampling points. Therefore, how to reduce the truncation errors and reconstruct the far-field radiation pattern of the AUT with fewer initial sampling points is of great importance.

A spiral scanning method was proposed to effectively reduce the near-field sampling time [1], [2]. The authors in [3]-[5] described an adaptive sampling method to determine the quasi-minimal distribution of the data samples obtained in the data grid, so as to represent the overall radiation characteristics. The authors in [6] proposed a method of using a switch probe for uniform data sampling with interpolation. A fast and effective pattern reconstruction method through clustering analysis and adaptive sampling was proposed for spherical near-field measurement systems in [7], [8]. The works provide some important ideas for conducting clustering analysis and data interpolation for the planar near-field measurement system.

Unlike the spherical near-field measurement system, e.g., [9], truncation errors are introduced in the planar near-field test due to the limited angular coverage of the scanning area. In order to reduce the impact of truncation errors on the measurement results, it is necessary to include a larger effective antenna radiation region by increasing the measurement area. However, increasing the measurement area means increasing the measurement samples and scanning time. Thus, it is vital to find a way to reduce the planar near-field truncation errors without increasing the measurement area.

To this end, the authors in [10], [11] introduced a smooth window function to filter the edge of the planar near-field data. Although this method reduces the influence of truncation errors, it also reduces the area of the effective region, which limits its performance. The source reconstruction method was adopted in [12]-[16] to get the equivalent current sources on the AUT aperture, based on which numerical analysis and pattern reconstruction were carried out. But this method is time-consuming for electrically large antennas. The band-limited signal extrapolation method has been widely used in the field of microwave detection and signal reconstruction [17]-[19]. Based on this foundation, the Gerchberg-Papoulis (GP) iterative algorithm was utilized in [20]-[24] to effectively reduce the truncation errors of the planar measurement without increasing the scanning range.

In this paper, we classify the limited initial sampling points by the K-means clustering method [25], [26], and calculate the area of each Voronoi tessellation cell and the gradient between adjacent sampling points. Then the area and gradient parameters under different weights are used to judge the deep and shallow interpolation regions within each cluster, in order

This work was supported in part by the National Natural Science Foundation of China under Grant 62171362. (*Corresponding author: Xiaoming Chen*)

J. Zheng, X. Chen is with the School of Information and Communication Engineering, Xi'an Jiaotong University, Xi'an 710049, China (e-mail: xiaoming.chen@mail.xjtu.edu.cn).

Y. Huang is with the Department of Electrical Engineering and Electronics, University of Liverpool, Liverpool L69 3GJ, UK.

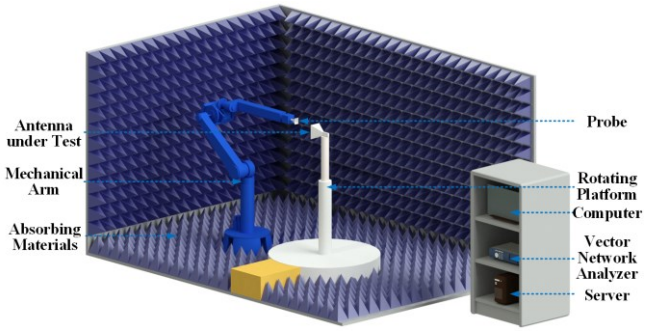

Fig. 1. Near-field antenna measurement environment.

to get more accurate interpolation results. Meanwhile, the GP iterative algorithm is used to reduce the truncation errors of the interpolated planar near-field data. The proposed method can reduce the measurement time to one-third of that of the conventional planar near-field measurement method with competitive accuracy performance.

II. THEORY

This section presents the method of antenna pattern reconstruction based on a small number of sampling points. First, the theories of clustering initial samples and Voronoi cell calculation are described. Then, a method of interpolating the initial sampling points according to different criteria is introduced. After that, the GP iterative algorithm which can reduce the truncation errors is explained. Finally, the reconstructed planar far-field pattern is obtained. We present the planar near-field antenna measurement procedure in detail next.

The discrete grid is first generated on the near-field sampling plane, on which a small number (N_{sample}) of initial sampling points are randomly selected. These initial sampling points are recorded as $X_1 = \{x_1, x_2, ..., x_{N_{sample}}\}$. In order to get appropriate interpolation results in different regions through the data characteristics of the initial sampling points, it is required to cluster these N_{sample} sampling points. In this work, the K-means unsupervised machine learning algorithm [7], [8] is used to classify these initial samples. This method calculates the 2-norm of the E-field vector difference (i.e., Euclidean distance) between each sample value and the cluster center, and classifies the sample into a cluster corresponding to the minimum difference. Now, suppose that there are k clusters, and the *j*-th cluster is marked as C_j $(1 \le j \le k)$ whose cluster center is

$$c_j = \frac{1}{n_j} \sum_{i \in C_j} x_i \tag{1}$$

where n_j represents the number of samples in the *j*-th cluster C_j. The procedure is repeated until the convergence is reached and the center is stable. Then calculates the sum of squares of errors (SSE) of all current clusters

$$F_k = \sum_{j=1}^{k} \sum_{i \in C_j} \left\| x_i - c_j \right\|^2 \tag{2}$$

Select different number of clusters k and recalculate the c_j and F_k values using (1) and (2), respectively. When the SSE curve has a significant inflection point at a certain k value, the optimal k is obtained.

After getting the cluster classification, it is necessary to carry out appropriate interpolation based on the initial data characteristics inside the corresponding clusters. The main parameters for evaluating the data interpolation method include the distribution density and the variation rate of the samples. The sample distribution density can be determined by calculating the cell area of all initial sampling points under the Voronoi tessellation [7]. If adjacent sampling points have common cell walls and vertices, then the field intensity gradient between the points can represent the variation rate of the sampling data.

The measurement region is discretized into Voronoi tessellation, so that each initial sampling point corresponds to a cell. Among these cells, the large one indicates that the area around the sampling point belongs to the under-sampling region. Thus, it is needed to increase the number of samples in this region. Each sampling point x_n $(n = 1, 2, ..., N_{sample})$ has a cell area of $A(x_n)$, and the distribution density $S(x_n)$ near the sampling point x_n can be expressed as follows

$$S(x_n) = \frac{A(x_n)}{A(x_1) + A(x_2) + ... + A(x_{N_{sample}})} \tag{3}$$

In order to calculate the gradient near the sampling point x_n , we first select the adjacent sampling point x_m that has common cell walls or vertices with the cell of the sampling point x_n , and then calculate the field strength gradient between x_m and x_n

$$\left| \nabla E_{(x_n, x_m)} \right| = \sqrt{\left(\frac{\partial E_{(x_n, x_m)}}{\partial x} \right)^2 + \left(\frac{\partial E_{(x_n, x_m)}}{\partial y} \right)^2} \tag{4}$$

where $\left| \nabla E_{(x_n, x_m)} \right|$ represents the absolute value of the field strength variation. The field strength gradient of other sampling points adjacent to x_n can be calculated in a similar way. The summation of the absolute values of all the gradients near x_n is denoted as $B(x_n)$

$$B(x_n) = \sum_{m=1}^{M_{sample}} \left(\left| \nabla E_{(x_n, x_m)} \right| \right) \tag{5}$$

where M_{sample} represents the total number of adjacent sampling points with common cell walls or vertices with x_n . The normalized gradient parameter $G(x_n)$ is given as

$$G(x_n) = \frac{B(x_n)}{B(x_1) + B(x_2) + ... + B(x_{N_{sample}})} \tag{6}$$

where $G(x_n)$ represents the overall normalized electric field gradient near the sampling point x_n. A large $G(x_n)$ implies

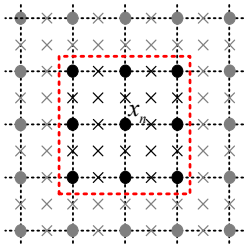

Fig. 2. Planar near-field interpolation method.

that the electric field near the sampling point x_n varies greatly and belongs to a highly dynamic region, and, therefore, more interpolation data should be added to this area. On the contrary, a small $G(x_n)$ indicates a slowly varying region and the interpolation can be reduced.

Combining the above two evaluation parameters $S(x_n)$ and $G(x_n)$, the following overall evaluation parameters $J(x_n)$ can be obtained

$$J(x_n) = h_1(1+S(x_n)) + h_2(1+G(x_n)) \tag{7}$$

where h_1 and h_2 (satisfying $h_1 + h_2 = 1$) are the weighting coefficients of area and gradient parameters, respectively. If $J(x_n)$ is large, more interpolation data need to be added to this area. The values of h_1 and h_2 are adjusted according to the cluster classified by (1) and (2), that is, if $G(x_n)$ in a cluster is too large, then it means that the overall cluster belongs to a highly dynamic region, and it is difficult to select an under-interpolated region from $G(x_n)$ in such a cluster. Therefore, in order to better judge whether more interpolation data needs to be added, h_1 can be increased in this cluster to get an area-oriented evaluation criterion and get reasonable interpolation results.

The deep and shallow interpolations are used in this work to interpolate the large and small cases of $J(x_n)$. As shown in Fig. 2, a deep interpolation gets 24 points (circle and fork) of the data around x_n on a uniform grid, while a shallow interpolation only needs to supplement the data of 8 points (circle) around x_n. Since the initial dataset X_1 is incomplete, the accurate deep and shallow interpolation points should be acquired from a complete sampling dataset X_2 with a larger sampling interval, which is less time-consuming. Thus, by performing the above interpolation operation on the $N_1 \times N_1$ uniform grid, the initial dataset X_1 can be extended to $(2N_1-1)\times(2N_1-1)$ uniform grid, and the number of the overall effective interpolated data N_{k_1} satisfies $N_{Sample} < N_{k_1} < (2N_1-1)(2N_1-1)$.

In order to reduce the influence of truncation errors in the planar near-field test, the GP iterative algorithm [20], [21] is used to extrapolate the visible planar near-field region in order to improve the accuracy of the interpolated far-field pattern. To begin with, the interpolated planar E-field is transformed by a two-dimensional Fourier transformation to obtain the

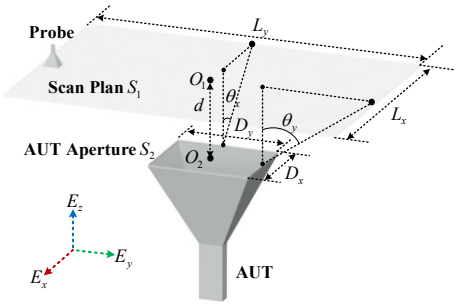

Fig. 3. Planar near-field scanning geometric parameters.

corresponding plane-wave spectrum (PWS)

$$P_{x,y}(k_x,k_y) = \frac{1}{2\pi}\iint E_{x,y}(x,y,d)e^{j(k_x x+k_y y)}e^{jk_z d}dxdy \tag{8}$$

where $E_{x,y}(x,y,d)$ is the planar electric field intensity after the process of (1)-(7) along the x and y directions at a distance d from the antenna aperture, $e^{jk_z d}$ transforms the observation plane from the scanning plane back to the antenna aperture,

$k_z = \sqrt{k^2 - k_x^2 - k_y^2}$, $k = 2\pi f_0 / c$

$$\begin{cases} k_x = m(dk_x) = m\dfrac{\pi}{M\Delta x} \\ k_y = n(dk_y) = n\dfrac{\pi}{N\Delta y} \end{cases} \tag{9}$$

where $m = 1,2,...,M$, $n = 1,2,...,N$, M and N representing the number of Fourier transformation points along the x and y axes, Δx and Δy denoting the scanning intervals of the near-field plane that are smaller than half-wavelength.

The scanning geometric parameters are shown in Fig. 3, where L_x and L_y are the length and width of the scanning plane S_1, respectively, D_x and D_y are the dimensions of the antenna aperture S_2, O_1 and O_2 are the centers of S_1 and S_2, respectively, $\theta_x = \arctan((L_x - D_x)/2d)$, and $\theta_y = \arctan((L_y - D_y)/2d)$ [27].

It can be known from [20], [21] that the far-field pattern derived from the truncated near-field scanning plane is reliable only in the region surrounded by rays passing through the edge of the antenna aperture and the scanning plane. The reliable region in the spatial domain is transformed into the wavenumber domain by Fourier transformation, and the region in the wavenumber domain can be defined by the following formula

$$U_0 = \left\{ \frac{k_x^2}{(k\sin\theta_x)^2} + \frac{k_y^2}{k^2} < \eta_x \right\} \cap \left\{ \frac{k_x^2}{k^2} + \frac{k_y^2}{(k\sin\theta_y)^2} < \eta_y \right\} \tag{10}$$

where θ_x and θ_y are the intersection angle of the reliable region (cf. Fig. 3); η_x and η_y should be greater than 1 in order to take more modes into account [21]. Thus, the data within U_0 belong to the reliable data to be retained. Otherwise, the data need to be filtered out. Accordingly, the spectral filtering can

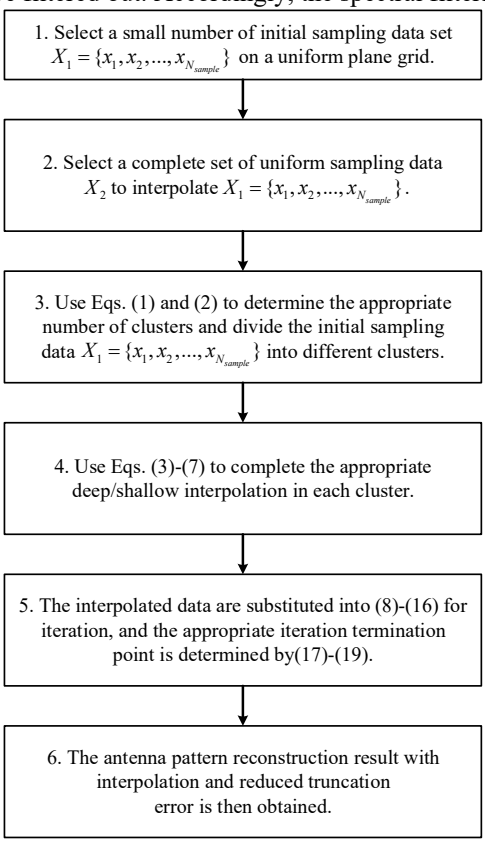

Fig. 4. Flow chart of the proposed method.

be expressed as

$$U_R = \begin{cases} 1, & (k_x, k_y) \in U_0 \\ 0, & (k_x, k_y) \notin U_0 \end{cases} \tag{11}$$

The filtered spectrum can be obtained by combining the PWS of Eqs. (8) and (11) as

$$P^{n+1}_{x,y(U_R)}(k_x, k_y) = U_R P^0_{x,y}(k_x, k_y) + P^n_{x,y}(k_x, k_y)\left[1 - U_R\right] \tag{12}$$

where n is the value of iteration times, $P^0_{x,y}(k_x, k_y)$ is the initial PWS of Eq. (8). The E-field intensity on the antenna aperture can be derived by the inverse Fourier transformation

$$E^{n+1}_{x,y}(x, y, 0) = \frac{1}{2\pi} \iint P^{n+1}_{x,y(U_R)}(k_x, k_y) e^{-j(k_x x + k_y y)} dk_x dk_y \tag{13}$$

After the inverse Fourier transformation to the spatial domain is done, the sampled values outside the AUT aperture are set to zero and the remaining values inside the aperture are retained to realize the spatial filtering. Namely, the filtering in the spatial domain is defined as

$$U_{AUT} = \begin{cases} 1, & (x, y) \in S_2 \\ 0, & (x, y) \notin S_2 \end{cases} \tag{14}$$

Then the E-field on the antenna aperture after spatial filtering can be expressed as

$$E^{n+1}_{x,y(U_{AUT})}(x, y, 0) = U_{AUT} E^{n+1}_{x,y}(x, y, 0) \tag{15}$$

After the filtering of the wavenumber domain and spatial domain in **Error! Reference source not found.**-(15) is done, the E-field intensity on the antenna aperture should be transformed by the Fourier transformation to get the corresponding PWS

$$P'_{x,y}(k_x, k_y) = \frac{1}{2\pi} \iint E^{n+1}_{x,y(U_{AUT})}(x, y, 0) e^{j(k_x x + k_y y)} dxdy \tag{16}$$

Next, $P^n_{x,y}(k_x, k_y)$ in Eq. **Error! Reference source not found.** is replaced by $P'_{x,y}(k_x, k_y)$ to obtain the PWS with reduced truncation errors through multiple iterations. However, the above calculation processes need to be executed under a limited number of iterations, thus it is necessary to select an appropriate termination point. Since the different PWS components satisfy

$$P_z(k_x, k_y) = -\frac{1}{k_z}\left(P_x(k_x, k_y)k_x + P_y(k_x, k_y)k_y\right) \tag{17}$$

Therefore, $P'_z(k_x, k_y)$ can be obtained by substituting $P'_{x,y}(k_x, k_y)$ into Eq. (17). Accordingly, the far-field pattern can be acquired by substituting the entire $P'_{x,y,z}(k_x, k_y)$ into the following formula

$$E_{x,y,z}(\theta, \varphi) = j \frac{e^{-jkr}}{2\pi r} k \cos\theta P'_{x,y,z}(k_x, k_y) \tag{18}$$

where $0 < r < \infty$, $k_x = k \sin\theta \cos\varphi$, and $k_y = k \sin\theta \sin\varphi$.

It has been revealed in [20] that the initial value in the reliable region consists of both accurate and erroneous solution parts. After several iterations, the accurate solution gradually converges while the erroneous part diverges, causing the overall error to decrease at the beginning and then increase. In this work, the optimal iteration termination point is determined by comparing the difference of the far-field pattern energy corresponding to different sampling points under different iteration times.

According to (17) and (18), *Num* -times iterations are performed on the planar near-field $E_{x,y}(x, y, d)$ and the number of interpolated data is N_{k_1}, the corresponding far-field is $E^1_{x,y,z,n_1}(\theta, \varphi)$, $n_1 = 1, ...Num$. Meanwhile, we extract N_{k_2} data from $E_{x,y}(x, y, d)$, and *Num* -times iterations are executed to get the far-field pattern $E^2_{x,y,z,n_2}(\theta, \varphi)$, $n_2 = 1, ...Num$. The difference of the far-field pattern energies under two datasets is expressed as

$$E_{(n_1,n_2)} = \iint \left| E^1_{x,y,z,n_1}(\theta, \varphi) - E^2_{x,y,z,n_2}(\theta, \varphi) \right|^2 \sin\theta d\theta d\varphi \tag{19}$$

For the near-field measurement in the same scanning plane, different data subsets have their own stable convergence points

after applying the same iterative process, that is, before the optimal convergence point, the accurate solution occupies the main component in the iterative result of (16), then the error component begins to increase gradually, and the minimum energy difference is obtained at the optimal termination point [20]. After finding the minimum energy difference $E_{(n_1,n_2)}$ of the first Num-times iterations, the current iteration numbers n_1 and n_2 (with a minimum $E_{(n_1,n_2)}$) are taken as the optimal

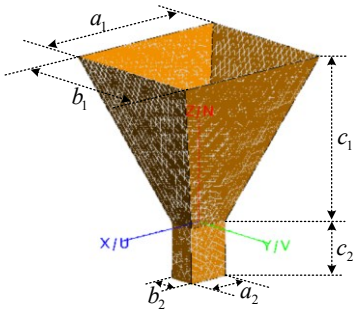

Fig. 5. Configuration of the AUT.

TABLE I
ANTENNA MODELING PARAMETERS

Horn size/mm		Waveguide size/mm	
a_1	31.90	a_2	8.00
b_1	27.90	b_2	5.00
c_1	30.00	c_2	10.00

TABLE II
MEANING OF EACH VARIABLES

Variable	Explanation
X_1	Initial randomly selected dataset to be interpolated
X_2	Basic dataset used to interpolate X_1
X_3	Dataset after the process of interpolation
$X_3^{'}$	Dataset after the process of GP algorithm
X_4	Complete sampling dataset used for comparison with $X_3^{'}$
X_5 , X_6	Subsets used to calculate the iteration termination point

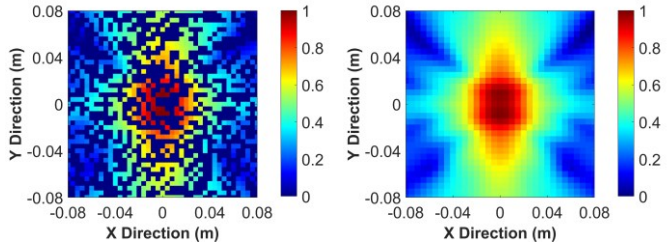

(a) (b)

Fig. 6. Distribution of the planar E-field strength of (a) the initial dataset X_1 and (b) the complete uniform dataset X_2.

iteration termination points of $E^1_{x,y,z,n_1}(\theta,\varphi)$ and $E^2_{x,y,z,n_2}(\theta,\varphi)$, respectively.

In order to elaborate on the steps of the proposed method, the processes of interpolation reconstruction and truncation error reduction are summarized in Fig. 4. It is known that more useful planar near-field data can be acquired by interpolating the incomplete initial sampling dataset, and the amount of data satisfies $N_{Sample} < N_{k_1} < (2N_1-1)(2N_1-1)$. Additionally, the proposed method makes the extrapolation through the GP algorithm in order to improve the accuracy of the solution in the reliable region and reduce the impact of the truncation errors.

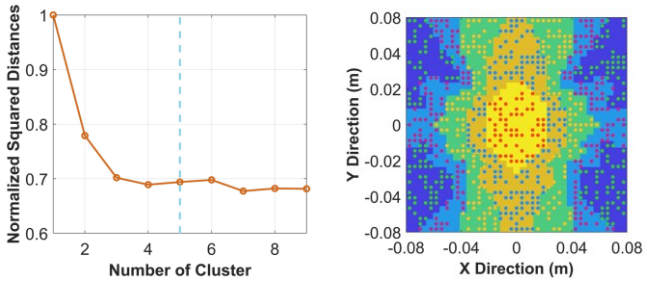

(a) (b)

Fig. 7. K-means clustering (a) L-curve (b) clustering result.

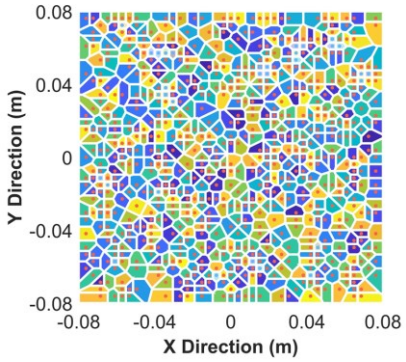

Fig. 8. Voronoi cell under deep and shallow interpolation classification.

III. SIMULATIONS AND MEASUREMENTS

Simulations and measurements are carried out in order to show the effectiveness of the proposed method. The full-wave simulations in this work are conducted using the commercial software FEKO.

A. Simulations

The FEKO model of the AUT is shown in Fig. 5, and the corresponding model parameters are listed in Table I. Table II shows the explanations of the datasets referred to in the following text in order to give clearer guidance. Without loss of generality, a working frequency of 30 GHz is chosen. The voltage amplitude on the waveguide port is normalized. The gain of the AUT is 18 dBi. The distance d between the near-field scanning plane S_1 and the antenna aperture S_2 is 5λ (where λ denotes the wavelength). The sampling plane S_1 is uniformly meshed, and the grid intervals along the x and y axes are Δx and Δy, respectively.

In order to obtain the initial sampling dataset $X_1 = \{x_1, x_2, ..., x_{N_{sample}}\}$, the sampling interval is set to $\Delta x = \Delta y = 4$ mm resulting in a 41×41 uniform grid, and 750

sampling points are randomly selected on the grid as the initial sampling set $X_1 = \{x_1, x_2, ..., x_{N_{sample}}\}, N_{sample} = 750$. The interpolation of the initial sampling points is executed on a complete basic dataset X_2 . Therefore, the sampling interval is adjusted to $\Delta x = \Delta y = 5$ mm and a 33×33 uniform basic dataset X_2 is obtained. The above process completes

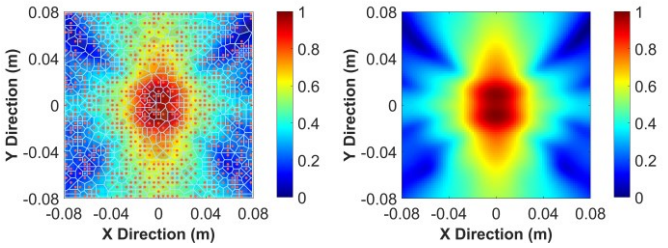

(a) (b)

Fig. 9. Planar near-field strength distribution of (a) the interpolated dataset X_3 and (b) the complete uniform dataset X_4 .

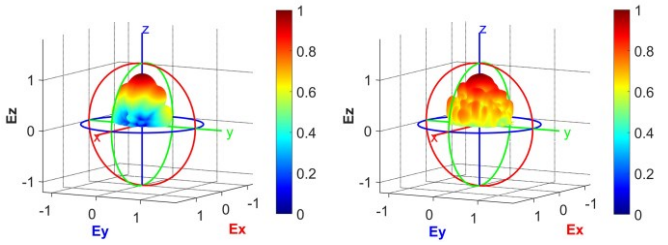

(a) (b)

(c)

Fig. 10. Comparison of the AUT radiation pattern after the interpolation including the (a) theoretical pattern, (b) X_1 NFT pattern, and (c) X_3 NFT pattern.

steps 1 and 2 in Fig. 4.

Figs. 6(a) and (b) show the planar E-field strength distributions of the initial sampling dataset X_1 and the uniform grid dataset X_2 , respectively. The data clustering is performed following step 3 in Fig. 4. X_1 is classified by the K-means method using Eqs. (1) and (2), and the cluster number k varies from 1 to 9. The SSE associated with each k value is calculated to obtain the L-curve (elbow curve) shown in Fig. 7(a). As can be seen in the L-curve, when $k = 5$, the overall SSE has a significant inflection point, and the subsequent values tend to be stable. Therefore, the optimal cluster number is $k = 5$. Correspondingly, X_1 is classified into 5 categories and the clustering results are shown in Fig. 7 (b).

After the clustering results are obtained, we calculate the corresponding Voronoi cells for all sampling points of X_1 , and the cell division results are shown in Fig. 8. The area and gradient of each cell are calculated according to Eqs. (3)-(6).

In the highly dynamic regions, such as the yellow and orange areas in Fig. 7(b), the weight of h_1 in Eq. (7) should be increased in order to better classify the deep and shallow

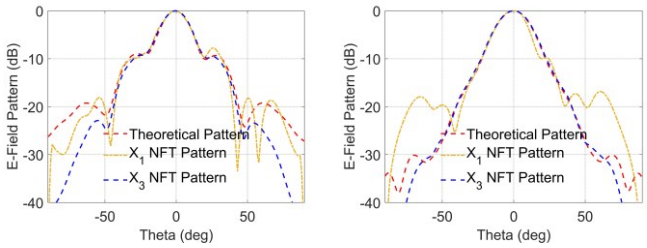

(a) (b)

Fig. 11. Comparison of the AUT radiation pattern after the interpolation in (a) E-plane and (b) H-plane.

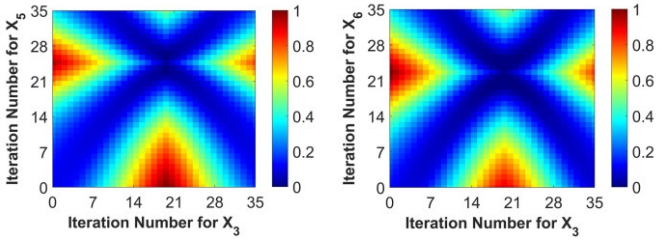

(a) (b)

Fig. 12. Normalized far-field energy difference between (a) X_3 and X_5 ; (b) X_3 and X_6 .

interpolation regions. By judging the cell parameters of each sampling point in X_1 , the deep and shallow interpolation regions are determined and marked by dark color (cell core is red) and light color (cell core is blue) respectively, as shown in Fig. 8.

Using the interpolation method shown in Fig. 2, the initial dataset X_1 is linearly interpolated with the basic dataset X_2 , and the extended dataset X_3 is obtained consequently. The interpolation process is executed in MATLAB. The new dataset X_3 has 6249 effective sampling points, i.e. $N_{k_1} = 6249$. Meanwhile, all the points of X_3 are arranged on the 81×81 uniform grid, where the empty grid is set to the mean values of its closest 8 points. Then X_3 becomes a 81×81 array. Finally, Fig. 9(a) can be obtained where the Voronoi cells and cell cores are also displayed. By observing the results, it can be seen that most grid points have corresponding interpolation data of X_3 . Only a few discrete points lack interpolation data, but this has little impact on the reconstruction effectiveness of the AUT pattern. In order to compare with the result of X_1 after the process of interpolation and GP algorithm, Δx and Δy is reset to 2 mm in FEKO to acquire the 81×81 uniform sampling dataset X_4 , whose planar E-field strength is shown in Fig. 9(b).

In order to show the effectiveness of the interpolation method, the near-to-far-field transformation (NFT) pattern of X_3 should be compared with the theoretical AUT pattern. Fig. 10 shows the three-dimensional (3D) theoretical pattern, X_1 NFT pattern and X_3 NFT pattern. It can be seen that the interpolation process adds more accurate data to the initial

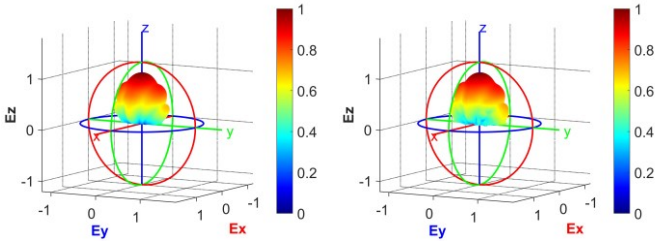

(a) (b)

Fig. 13. Comparison of the AUT radiation pattern after the GP algorithm including the (a) X_4 NFT pattern, and (b) $X_3^{'}$ NFT pattern.

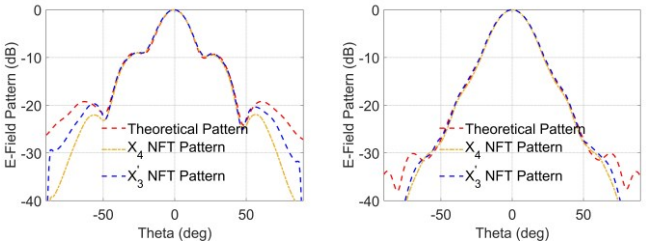

(a) (b)

Fig. 14. Comparison of the AUT radiation pattern after the GP algorithm in (a) E-plane and (b) H-plane.

dataset X_1, and the interpolated result X_3 has a better accuracy than the X_1. Fig. 11 shows the E-plane and H-plane of the patterns in Fig. 10. It can be known that the interpolation method increases the number of effective data in X_1 and the reconstruction accuracy, but the truncation errors need to be further improved by GP algorithm.

Next, we uniformly extract the 33×33 and 41×41 planar near-field data subsets from X_3, which are recorded as X_5 and X_6, respectively. According to steps 5 and 6 in Fig. 4, X_3, X_5 and X_6 should be iterated, and the normalized far-field energy differences between X_3 and X_5, and X_3 and X_6 are obtained by Eq. (19), as shown in Figs. 12(a) and (b). The horizontal coordinate represents the iteration times of X_3, while the vertical coordinates of Figs. 12(a) and (b) represent the iteration times of X_5 and X_6, respectively.

By searching the minimum $E_{(n_1,n_2)}$ of the 35-times iterations, it can be found that the optimal iteration termination point for the dataset X_3 is 20. In addition, by comparing the far-field energy iteration differences corresponding to different data subsets of X_3 in Figs. 12(a) and (b), it can be seen that Eq. (19) can effectively find the minimum far-field energy difference between X_3 and the other two subsets, and the iteration termination point of X_3 is relatively stable.

Finally, the planar near-field data X_3 after 20 iterations is recorded as $X_3^{'}$, and then the reconstructed AUT pattern is obtained by the NFT algorithm. Fig. 13 shows the NFT pattern of the dataset X_4 and the reconstructed dataset $X_3^{'}$, where

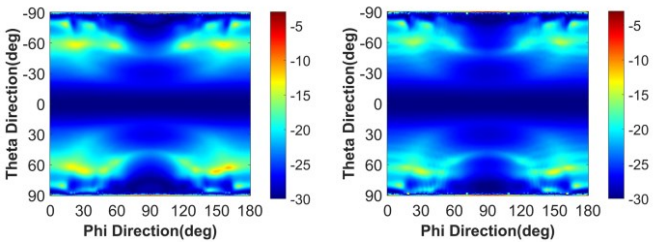

(a) (b)

Fig. 15. The normalized radiation pattern errors between theoretical pattern and (a) X_4 NFT pattern (b) $X_3^{'}$ NFT pattern.

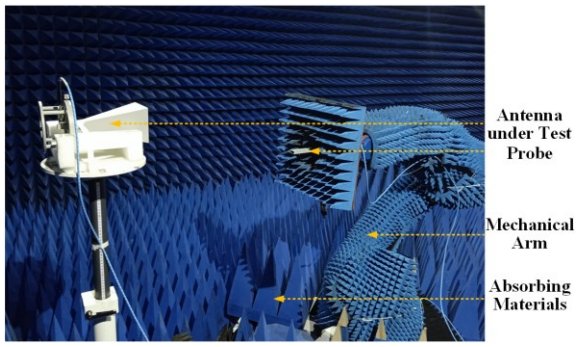

Fig. 16. The planar near-field measurement environment.

$\theta = \varphi = 1^{\circ}$. The antenna gain of the reconstructed $X_3^{'}$ is 16.8 dBi. Meanwhile, the E-plane and H-plane of the theoretical pattern, X_4 NFT pattern and $X_3^{'}$ NFT pattern are drawn in Fig. 14, where the theoretical pattern is the same as Fig. 10(a).

Comparing the results in Figs. 10, 11, 13 and 14, it can be seen that the initial sampling dataset X_1 with 750 points cannot characterize all the E-field strength of the AUT, which consequently is very different from the theoretical pattern. Besides, after the process of interpolation and GP algorithm, the $X_3^{'}$ NFT pattern has a better improvement in truncation error than the X_3 NFT pattern, and has good consistency with the theoretical pattern, as shown in Figs. 11 and 14.

Moreover, Fig. 15 shows the entire normalized far-field energy errors between the theoretical pattern of Fig. 10(a) and the NFT pattern of datasets X_4 and $X_3^{'}$ of Figs. 13(a) and (b), respectively. The results clearly reveal that the far-field pattern of the AUT after the interpolation and GP iterative processes has less errors and better consistency with the theoretical value.

B. Measurements

In this section, the method described in this paper is verified in the planar near-field test environment shown in Fig. 16. The horn antenna with the gain of 15.5 dBi is selected as AUT1, the working frequency is 4.5 GHz and the distance between the

scanning plane and the antenna aperture is 5λ . The horn aperture size is 11.9 cm × 16.8 cm. The scanning interval is set to $\Delta x = \Delta y = 21.6$ mm, and collect 400 initial sampling data under the 31×31 uniform grid as X_1 . Readjust the scanning interval to $\Delta x = \Delta y = 32.5$ mm and acquire a complete 21×21

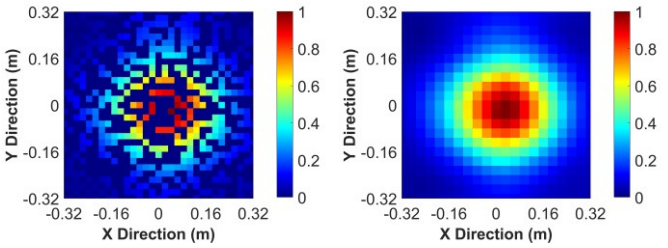

(a) (b)

Fig. 17. Distribution of the measured planar E-field strength of (a) the initial dataset X_1 and (b) the complete uniform dataset X_2 .

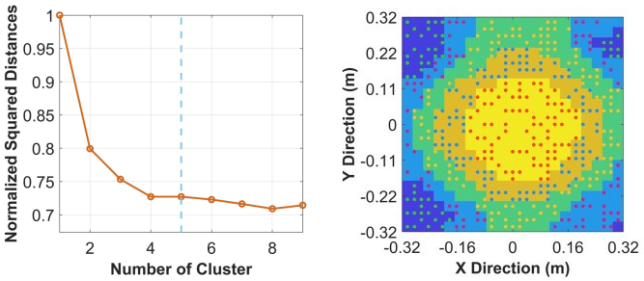

(a) (b)

Fig. 18. Measured K-means clustering (a) L-curve (b) clustering result.

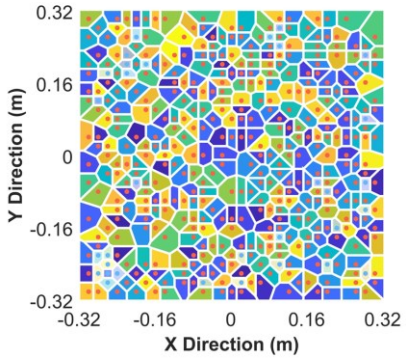

Fig. 19. Voronoi cell under deep and shallow interpolation classification.

basic dataset X_2 . The near-field sampling results are shown in Fig. 17. The L-curve of X_1 is shown in Fig. 18(a), and the clustering result with $k = 5$ is shown in Fig. 18(b).

The Voronoi cells classification is shown in Fig. 19. The interpolated new dataset X_3 (Fig. 20(a)) has 3551 effective sampling points. The dataset X_4 (Fig. 20(b)) with 61×61 grid points is acquired by setting the sampling interval to $\Delta x = \Delta y = 10.8$ mm.

The 3D comparison of the theoretical pattern, X_1 NFT pattern and X_3 NFT pattern is shown in Fig. 21, where the theoretical far-field is the NFT pattern measured in the multi-probe anechoic chamber (AC), which can be less affected by the truncation errors. The E- and H-plane of the radiation patterns in Fig. 21 are shown in Fig. 22. From the results, it is clear that the interpolation method can increase the effective data and get a well-reconstructed pattern of X_3 .

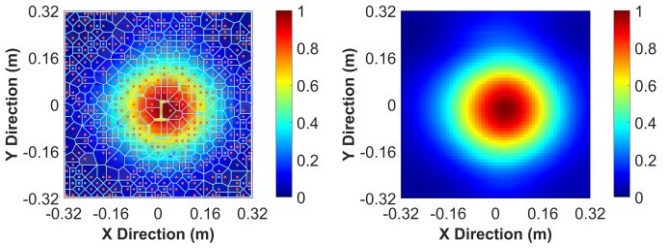

(a) (b)

Fig. 20. The measured AUT1 planar near-field strength distribution of (a) the interpolated dataset X_3 and (b) the complete uniform dataset X_4 .

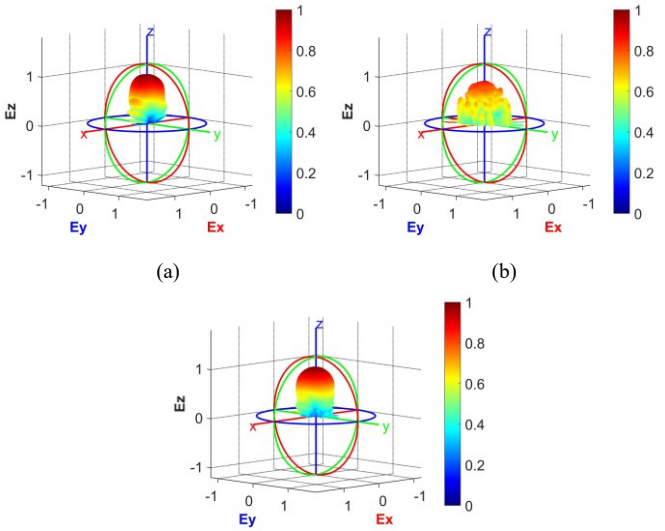

(a) (b)

(c)

Fig. 21. Comparison of the measured AUT1 radiation pattern after the interpolation including the (a) theoretical pattern, (b) X_1 NFT pattern, and (c) X_3 NFT pattern.

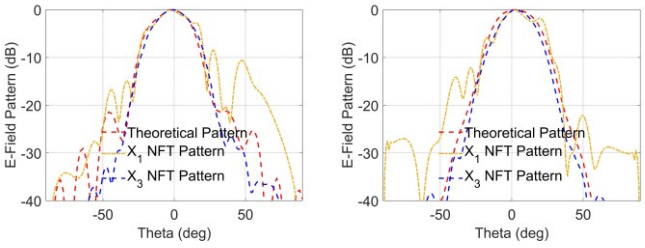

(a) (b)

Fig. 22. Comparison of the measured AUT1 radiation pattern after the interpolation in (a) E-plane and (b) H-plane.

After the interpolation process, the GP algorithm needs to be executed to reduce the truncation errors. Datasets X_5 and X_6 are uniformly extracted from X_3 , and the normalized far-field energy differences are shown in Figs. 23(a) and (b). The optimal

number of the iterations of X_3 is 18.

The planar near-field data X_3 after 18 iterative operations is recorded as $X_3^{'}$, and Fig. 24 shows the 3D X_4 NFT pattern and $X_3^{'}$ NFT pattern. The reconstructed antenna gain is 13.2 dBi.

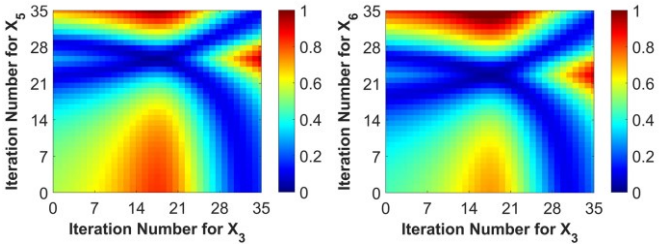

(a) (b)

Fig. 23. The normalized far-field energy difference between X_3 and (a) X_5 (b) X_6.

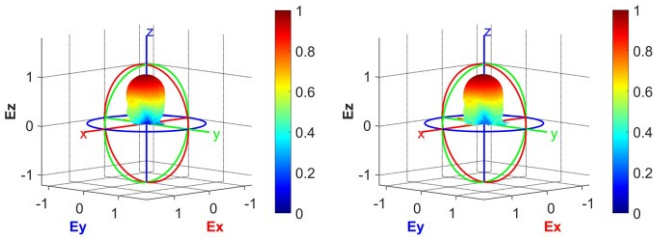

(a) (b)

Fig. 24. Comparison of the measured AUT1 radiation pattern after the GP algorithm including the (a) X_4 NFT pattern, and (b) $X_3^{'}$ NFT pattern.

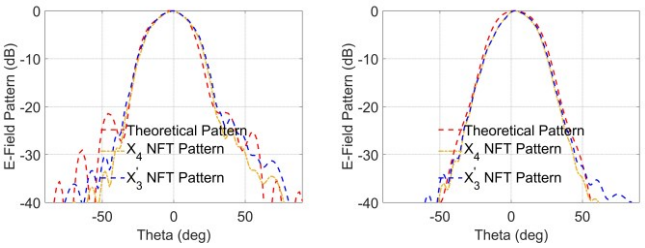

(a) (b)

Fig. 25. Comparison of the measured AUT1 radiation pattern after the GP algorithm in (a) E-plane and (b) H-plane.

Fig. 25 shows the E-plane and H-plane of the theoretical pattern (Fig. 21(a)), X_4 and $X_3^{'}$ NFT patterns. Fig. 26 shows the entire normalized far-field energy errors between Fig. 21 (a) and Figs. 24 (a) and (b) respectively. Through the results, it can be known that there are smaller errors between the NFT pattern of $X_3^{'}$ and the theoretical one.

In order to show the effectiveness of the proposed method for the AUT with higher gain and smaller size, we select an antenna with a gain of 20 dBi and aperture size of 10.6 cm × 13.6 cm as AUT2. The testing frequency is set to 8.6 GHz, and the distance between the sampling plane and aperture is 5λ. The interval Δx and Δy are both set to 17 mm, 11.3 mm and 5.7 mm to form the 21×21 (X_2), 31×31 and 61×61 (X_4), datasets, respectively, and we select 400 samples from the 31×31 grid to acquire X_1, as shown in Fig. 27. After the processes of the proposed method, $X_3^{'}$ can be derived. Since the 8.6 GHz is out of the frequency testing range in the multi-probe AC, then the far-field pattern of AUT2 is acquired in the planar far-field system. Therefore, the comparison of 3D radiation pattern is omitted here and the E-plane and H-plane are shown in Fig. 28. The reconstructed antenna gain is 17 dBi. From the measurement results, it is obvious that the proposed method can effectively reconstruct the AUT2 pattern with a small number of initial samples, and the truncation errors can also be reduced when compared with the X_4 having the same grid interval.

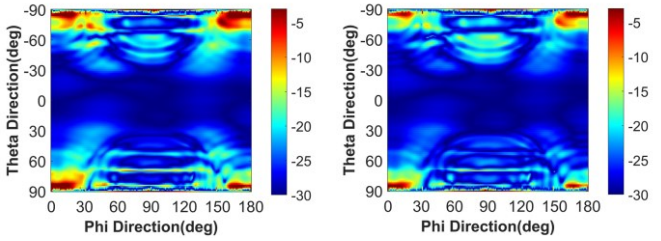

(a) (b)

Fig. 26. The measured normalized radiation pattern errors between theoretical pattern and (a) X_4 NFT pattern (b) $X_3^{'}$ NFT pattern.

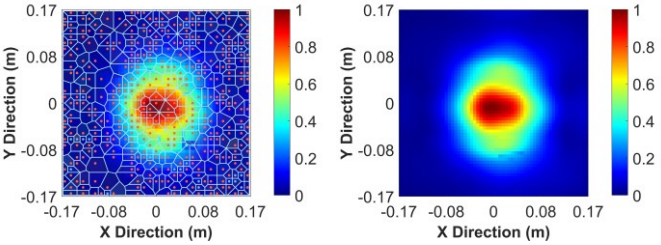

(a) (b)

Fig. 27. The measured AUT2 planar near-field strength distribution of (a) the interpolated dataset X_3 and (b) the complete uniform dataset X_4.

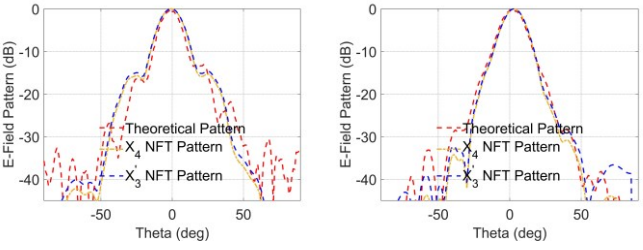

(a) (b)

Fig. 28. Comparison of the measured AUT2 radiation pattern after the interpolation and GP algorithm in (a) E-plane (b) H-plane.

C. *Discussions*

1) *Error Analysis*

In order to further discuss the accuracy of the proposed method, we use the following relative errors to show the difference between the theoretical pattern and the reconstructed pattern

$$D=\frac{\sum_{\theta=-180^{\circ}}^{180^{\circ}}\left|E_0(\theta,\varphi)-E_{recon}(\theta,\varphi)\right|^2}{\sum_{\theta=-180^{\circ}}^{180^{\circ}}\left|E_0(\theta,\varphi)\right|^2} \tag{20}$$

where $E_0(\theta,\varphi)$ and $E_{recon}(\theta,\varphi)$ are the theoretical and reconstructed patterns in E-plane and H-plane. Here we calculate the pattern errors in Figs. 11, 14, 22, 25 and 28, and the results are shown in Table III. The subscripts E and H represent the errors in E-plane and H-plane. The subscript 1-4 represent the errors between the theoretical pattern and X_1, X_3, X_4, and $X_3^{'}$ NFT pattern, respectively. Each two rows correspond to the pattern errors of E-plane and H-plane in one figure, and the figure number is shown in the first column.

TABLE III
RELATIVE ERRORS OF E-PLANE AND H-PLANE

Figure	Items	Value	Items	Value
Fig. 11	$D_{1,E}$	8.09%	$D_{1,H}$	11.81%
	$D_{2,E}$	6.67%	$D_{2,H}$	2.86%
Fig. 14	$D_{3,E}$	4.81%	$D_{3,H}$	2.45%
	$D_{4,E}$	4.21%	$D_{4,H}$	2.43%
Fig. 22	$D_{1,E}^{'}$	17.45%	$D_{1,H}^{'}$	22.03%
	$D_{2,E}^{'}$	10.04%	$D_{2,H}^{'}$	11.96%
Fig. 25	$D_{3,E}^{'}$	8.40%	$D_{3,H}^{'}$	10.95%
	$D_{4,E}^{'}$	6.99%	$D_{4,H}^{'}$	11.49%
Fig. 28	$D_{3,E}^{''}$	18.15%	$D_{3,H}^{''}$	13.53%
	$D_{4,E}^{''}$	15.04%	$D_{4,H}^{''}$	12.20%

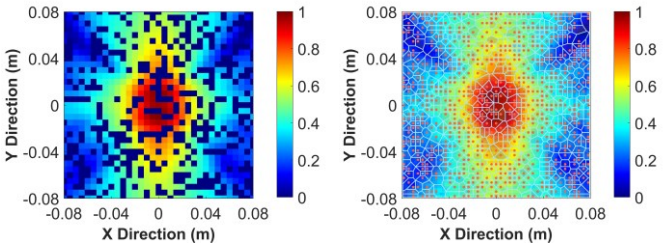

(a) (b)

Fig. 29. Distribution of the planar E-field strength of (a) the basic dataset X_2 and (b) the interpolated dataset X_3.

From the results, it can be concluded that the interpolation method can effectively increase the useful data of X_1 and improve the accuracy of the NFT pattern (see the comparison of D_1, D_2, $D_1^{'}$ and $D_2^{'}$ in E- and H-plane). Besides, after the process of the GP algorithm, the entire truncation errors are decreased and the NFT of $X_3^{'}$ is well consistent with the theoretical one (see the comparison of D_3, D_4, $D_3^{'}$, $D_4^{'}$, $D_3^{''}$ and $D_4^{''}$ in E- and H-plane). Thus, the proposed method can effectively reconstruct the AUT NFT pattern with good accuracy.

More importantly, in the measurement process, the overall measurement time of X_4 is 3 hours, while the time costs of X_2 and X_1 are 0.5 and 1 hour, respectively. Therefore, the proposed method not only reduces the number of initial samples, but also decreases the entire measurement time consumption, indicating that the proposed method is well efficient and practical.

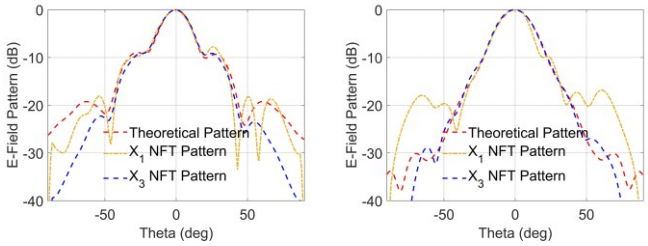

(a) (b)

Fig. 30. Comparison of the AUT radiation pattern after the interpolation in (a) E-plane and (b) H-plane.

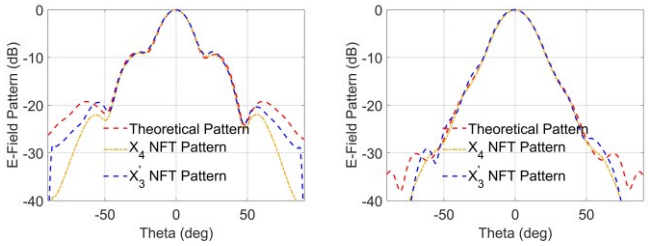

(a) (b)

Fig. 31. Comparison of the AUT radiation pattern after the GP algorithm in (a) E-plane and (b) H-plane.

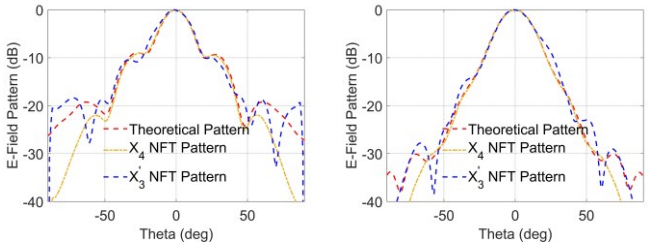

(a) (b)

Fig. 32. Comparison of the AUT radiation pattern after the interpolation and GP algorithm in (a) E-plane and (b) H-plane.

2) Sampling Method

In this work, we assume that the initial dataset X_1 is not completely sampled on a uniform grid due to arbitrary data failure and measurement restriction (e.g., mechanical arm movement range and test accuracy). This assumption accounts for a more general and complex measurement situation, since the random selection can simulate a much worse case of the sampling loss and data storage failure. However, the sampling method of X_1 and X_2 is not strictly limited to a specific form of random, uniform, or large-interval (larger than $\lambda/2$) sampling method. Here, we add two more cases to illustrate the effectiveness of the proposed method with randomly selected X_2 and the necessity of the basic dataset X_2.

First, we use the same simulation model in Fig. 5, and the

dataset X_2 is randomly selected on the 33×33 uniform grid. The total number of the selected samples of X_2 is 700, and the planar E-field strength of X_2 is shown in Fig. 29(a). Using the proposed interpolation method, the interpolated result (X_3) of X_1 is shown in Fig. 29(b). After the process of the GP algorithm, $X_3^{'}$ can then be acquired. Figs. 30 and 31 show the E-plane and H-plane of X_3 and $X_3^{'}$ NFT pattern, compared with the theoretical pattern, X_1 and X_4 NFT pattern. The relative errors $D_{2,E}^{r}$ and $D_{2,H}^{r}$ in Figs. 30(a) and (b) are 6.98% and 3.83%; $D_{4,E}^{r}$ and $D_{4,H}^{r}$ in Figs. 31(a) and (b) are 4.61% and 3.17% (the meaning of the subscript is the same as that in Table III). From the comparisons of Figs. 11, 14, 30, 31, and the relative errors, it can be known that the randomly selected X_2 can effectively supplement the useful data in X_1 , and the reconstructed AUT pattern is in good agreement with the theoretical one.

Then, we use X_1 to realize self-interpolation, and the E-plane and H-plane of the NFT results after the interpolation and GP algorithm can be derived as Fig. 32. When compared with Figs. 11, 14, 30, and 31, it is obvious that the effectiveness and performance of the self-interpolation method is not as good as the proposed method with a random or complete sampling of X_2 .

The above results reveal that: When X_1 and X_2 are both used in the random selection method, the two datasets are in different sampling intervals containing different values with different precisions, then X_2 can add more additional useful data to the initial dataset X_1 . If X_1 is interpolated by itself, then it is hard to supplement more useful data when the data loss is severe (i.e., the number of the initial samples of X_1 is too small). Therefore, X_2 is of great importance to the supplementation of useful data of X_1 and the effectiveness of the proposed method.

Notably, from the perspective of the stability of the measurement system, the stability is influenced by different factors, including whether the calibration within the testing frequency range of the vector network analyzer (VNA) is accurate enough, whether the software of the control computer is compatible with the control of the signal source and mechanical arm (i.e., acquisition issue), whether the interface between the GUI and background processing program is robust, etc. Accordingly, on the one hand, if the measurement of AUT is complicated, then the increase in the sampling number, time cost, and data storage will raise the burden of the system for data sampling and processing, leading to a higher probability of instability and data loss. Thus, in this case, the complete sampling of the smaller number of X_2 is easier to be realized than X_1 , and the selection of complete sampling of X_2 and random data loss of X_1 is more suitable and reasonable. On the other hand, if the system has poor robustness, the random sampling (representing random data loss) of X_1 and X_2 is more reasonable, and the effectiveness of the proposed method under this circumstance is verified, as shown in Figs. 29-31.

What is more, in order to enlarge the reliable region and improve the side lobes of the AUT, the near-field scanning area should be enlarged. Thus, when the working frequency of the AUT is increased, the number of the entire samples should be significantly increased and the measurement time of the initial dataset X_1 and the basic dataset X_2 is also increased. Therefore, although the proposed method performs well in different working frequencies, the measurement time and accuracy should be comprehensively considered when applying for the AUT with a higher gain or wider frequency range.

IV. Conclusion

This paper combines the clustering interpolation method with a small number of initial sampling points and the GP iterative algorithm for planar near-field measurements. The proposed planar near-field measurement method can reduce the number of initial samples, and acquire more appropriate regional data through clustering and interpolation. Notably, the practicability of the randomly selected method for the initial dataset has been verified in [7], and the random selection can also have a good effect on reducing the time cost of the current source reconstruction process [7], [15]. What's more, using the random sampling method to simulate the complex and unexpected data failure and measurement restriction is more reasonable and practical when compared with some specific even sampling method. In this way, the entire sampling time can be significantly reduced. Besides, the simulated and measured results reveal that the iterative algorithm can effectively decrease the influence of truncation errors on the interpolated planar measurement results. Consequently, the proposed method can reduce the measurement time to one-third of that of the conventional planar near-field measurement with equally good accuracies.

References

[1] F. D'Agostino, F. Ferrara, C. Gennarelli, R. Guerriero, S. McBride and M. Migliozzi, "Fast and accurate antenna pattern evaluation from near-field data acquired via planar spiral scanning," *IEEE Trans. Antennas Propag.*, vol. 64, no. 8, pp. 3450-3458, Aug. 2016.

[2] F. D'Agostino, F. Ferrara, C. Gennarelli, R. Guerriero and M. Migliozzi, "Experimental assessment of an effective near-field–far-field transformation with spherical spiral scanning for quasi-planar antennas," *IEEE Antennas Wireless Propag. Lett.*, vol. 12, pp. 670-673, 2013.

[3] F. D'Agostino, F. Ferrara, C. Gennarelli, et al., "A nonredundant near-field to far-field transformation with spherical spiral scanning for nonspherical antennas," *Open Elect. Electron. Eng. J.*, vol. 3, pp. 4-11, 2009.

[4] D. Deschrijver, K. Crombecq, H. M. Nguyen and T. Dhaene, "Adaptive sampling algorithm for macromodeling of parameterized s-parameter responses," *IEEE Trans. Microw. Theory Techn.*, vol. 59, no. 1, pp. 39-45, Jan. 2011.

[5] D. Deschrijver, F. Vanhee, D. Pissoort and T. Dhaene, "Automated near-field scanning algorithm for the EMC analysis of electronic devices," *IEEE Trans. Electromagn. Compat.*, vol. 54, no. 3, pp. 502-510, Jun. 2012.

[6] R. R. Alavi, R. Mirzavand and P. Mousavi, "Fast and accurate near-field to far-field transformation using an adaptive sampling algorithm and machine learning," in *Proc. Int. Symp. IEEE Antennas Propag. USNC-URSI Nat. Radio Sci. Meet.*, pp. 225-226, 2019.

[7] R. R. Alavi, R. Mirzavand, J. Doucette and P. Mousavi, "An adaptive data acquisition and clustering technique to enhance the speed of spherical near-field antenna measurements," *IEEE Antennas Wireless Propag. Lett.*, vol. 18, no. 11, pp. 2325-2329, Nov. 2019.

[8] R. R. Alavi and R. Mirzavand, "Range extension in partial spherical near-field measurement using machine learning algorithm," *IEEE Antennas Wireless Propag. Lett.*, vol. 19, no. 11, pp. 2003-2007, Nov. 2020.

[9] M. D. Migliore, F. Soldovieri, and R. Pierri, "Far-field antenna pattern estimation from near-field data using a low-cost amplitude-only measurement setup," *IEEE Trans. Instrum. Meas.*, vol. 49, no. 1, pp. 71-76, Feb. 2005.

[10] P. R. Rousseau, "The planar near-field measurement of a broad beam antenna using a synthetic subarray approach," *IEEE AP-S Symp. Digest*, vol. 1, no. 1, pp. 160-163, 1997.

[11] T. Al-Mahdawi, "Planar near-field measurement of low directivity embedded antennas using a synthetic array probe technique," *IEEE AP-S Symp. Digest*, vol. 3, pp. 1311-1314, 1998.

[12] O. M. Bucci and M. D. Migliore, "A new method for avoiding the truncation error in near-field antennas measurements," *IEEE Trans. Antennas Propag.*, vol. 54, no. 10, pp. 2940-2952, Oct. 2006.

[13] S. Gregson, C. G. Parini, and J. McCormick, "Development of wide-angle antenna pattern measurements using a probe-corrected polyplanar near-field measurement technique," *Proc. Inst. Elect. Eng. Microw. Antennas Propag.*, vol. 152, pp. 563-572, 2005.

[14] M. Serhir, J. Geffrin, A. Litman and P. Besnier, "Aperture antenna modeling by a finite number of elemental dipoles from spherical field measurements," *IEEE Trans. Antennas Propag.*, vol. 58, no. 4, pp. 1260-1268, Apr. 2010.

[15] P. Petre and T. K. Sarkar, "Planar near-field to far-field transformation using an equivalent magnetic current approach," *IEEE Trans. Antennas Propag.*, vol. 40, no. 11, pp. 1348-1356, Nov. 1992.

[16] J. Pérez and J. Basterrechea, "Analysis of different GA strategies applied to antenna far‐fields reconstruction from planar acquisition," *Microw. Opt. Tech. Lett.*, vol. 39, pp. 422-426, 2003.

[17] A. Papoulis, "A new algorithm in spectral analysis and band-limited extrapolation," *IEEE Trans. Circuits Syst.*, vol. 22, no. 9, pp. 735-742, Sep. 1975.

[18] J. M. Rius et al., "Planar and cylindrical active microwave temperature imaging: numerical simulations," *IEEE Trans. Med. Imag.*, vol. 11, no. 4, pp. 457-469, Dec. 1992.

[19] K. T. Kim, "Truncation-error reduction in 2D cylindrical/spherical near-field scanning," *IEEE Trans. Antennas Propag.*, vol. 58, no. 6, pp. 2153-2158, Jun. 2010.

[20] E. Martini, O. Breinbjerg and S. Maci, "Reduction of truncation errors in planar near-field aperture antenna measurements using the Gerchberg-Papoulis algorithm," *IEEE Trans. Antennas Propag.*, vol. 56, no. 11, pp. 3485-3493, Nov. 2008.

[21] X. Li, T. Zhang, M. Wei and L. Yang, "Reduction of truncation errors in planar near-field antenna measurements using improved Gerchberg–Papoulis algorithm," *IEEE Trans. Instrum. Meas.*, vol. 69, no. 9, pp. 5972-5974, Sept. 2020.

[22] R. W. Gerchberg, "Super-resolution through Error Energy Reduction," *Opti. Acta*, vol. 21, no. 9, pp. 709-720, 1974.

[23] E. Martini, O. Breinbjerg and S. Maci, "Reduction of truncation errors in planar near-field aperture antenna measurements using the method of alternating orthogonal projections," in *Proc. Eur. Conf. Antennas Propag., EuCAP*, Nice, France, 2006, pp. 1-6.

[24] E. Martini, O. Breinbjerg and S. Maci, "A convergence criterion for the iterative gerchberg-papoulis algorithm applied to truncation error reduction in planar near-field measurements," in *Proc. 2nd Eur. Conf. Antennas Propag., EuCAP 2007*, Edinburgh, U.K., 2007, pp. 1-7.

[25] B. Purnima and K. Arvind, "EBK-means: A clustering technique based on elbow method and K-means in WSN," *Int. J. Comput. Appl.*, vol. 105, no. 9, pp. 17-24, 2014.

[26] R. He, B. Ai, A. F. Molisch, G. L. Stüber, Q. Li, Z. Zhong, and J. Yu, "Clustering enabled wireless channel modeling using big data algorithms," *IEEE Commun. Mag.*, vol. 56, no. 5, pp. 177-183, May 2018.

[27] C. Parini , S. Gregson , J. Mccormick. *Principles of planar near-field antenna measurements*, London: IET, 2014.